Measurements of the Effect of Adiabat on Shell Decompression in Direct-Drive Implosions on OMEGA

In inertial confinement fusion (ICF), laser beams are used to implode a spherical shell of deuterium and tritium. To reach maximum compression and achieve fusion conditions, the fuel entropy must be minimized (close to the Fermi-degenerated limit).[1,2] This requires accurate control of the shocks and compression waves launched during the implosion.[3] The entropy in ICF is commonly characterized by the shell's adiabat (α) defined as the mass-averaged ratio of the shell's pressure to the Fermi-degenerated pressure.[4,5] One-dimensional (1-D) simulations suggest that reducing the adiabat increases the shell density and reduces shell thickness. At a low adiabat, however, short-scale nonuniformities amplified by the Rayleigh–Taylor (RT) instability lead to shell decompression, which increases its effective adiabat.[5–9] Therefore, optimizing the implosion performance requires a balance between minimizing the adiabat and reducing the RT growth to maintain a compressible shell.

The effect of the adiabat on shell compression has typically been studied by measuring its effect on integrated performance parameters (e.g., neutron yield and areal density). Recently, several studies have shown that increasing the adiabat of the shell improved the neutron yield in both direct-[10,11] and indirect-drive[12,13] configurations. For low-adiabat implosions, the nonuniformities were shown to result in the ablator mixing into the hot spot, which cooled the hot spot and reduced the fusion performance.[14,15] A threshold was observed in the calculated adiabat where, above the threshold, the measured areal density was recovered by 1-D simulations.[16] Previous research aimed at studying integrated implosions has used flux-limiter models,[11,17–19] but these models did not reproduce the mass ablation rate and the conduction-zone length correctly, which led to errors in the calculation of the laser imprint and the RT growth.[20]

This article presents the first measurements of the effect of adiabat on the shell decompression and the first hydrodynamic simulations[21] that reproduce the detailed experimental observables by including laser imprint[17] and cross-beam energy transfer (CBET)[22] models. The maximum in-flight shell thickness was obtained using a novel technique where the outer and inner surfaces of the shell were simultaneously measured using self-emission images of the imploding target. When the calculated adiabat of the shell was decreased from $\alpha = 6$ to $\alpha = 4.5$, the shell thickness was measured to decrease from 75 ± 2 μm to 60 ± 2 μm, but when the adiabat was decreased further to $\alpha = 1.8$, the shell thickness was measured to increase to 75 ± 2 μm. Over this adiabat range, the measured minimum core size continued to decrease, demonstrating that the decompression of the shell measured for low adiabats was not caused by errors in the adiabat calculations, but a result of the increase in the RT growth. The optimum performance (minimum shell thickness and maximum neutron yield) was obtained for $\alpha = 3$. In simulations that did not include laser imprint, the simulated thicknesses were close to measurements for $\alpha > 3$, but they significantly underestimated the shell thickness for $\alpha \leq 3$, which confirmed that the decompression measured for low adiabats was a result of laser imprint. The simulations that included state-of-the-art models reproduce the measured outer-shell trajectory, maximum in-flight shell thicknesses, inner-shell deceleration, minimum core size, and neutron yields and show that the increased shell thickness for $\alpha \leq 3$ is caused by laser imprint.

The experiments employed 60 ultraviolet ($\lambda_0 = 351$ nm) laser beams on the OMEGA laser.[23] The laser beams uniformly illuminated the target and were smoothed by polarization smoothing,[24] smoothing by spectral dispersion (SSD),[25] and distributed phase plates (fourth-order super-Gaussian with 95% of the energy contained within the initial target diameter).[26] On some shots, the laser imprint was increased by turning off SSD. A 100-ps-long picket and a $1.7\pm0.2 \times 10^{14}$-W/cm^2 foot on the rise of the drive pulse were used to set the adiabat of the shell.[9] They were followed by a 2-ns-long drive pulse that accelerated the target to its final velocity of ~200 km/s. The picket intensity was varied between 0.85×10^{14} W/cm^2 and 5.5×10^{14} W/cm^2 to vary the adiabat of the shell between 1.8 and 6. The total laser energy was 21 ± 0.3 kJ, which resulted in a maximum on-target overlapped intensity of $4.7\pm0.06 \times 10^{14}$ W/cm^2. The shells were made of 26.5 ± 0.2-μm-thick glow-discharge polymer (CH with a density of 1.03 g/cm^3) with an outer radius of 433 ± 4 μm and filled with 11 ± 0.5 atm of deuterium.

The recently developed self-emission x-ray imaging technique[27] was adapted to simultaneously measure the outer- and inner-shell trajectories (Fig. 147.1). The soft x rays emitted by the imploding target were imaged with an array of 10-μm-diam pinholes onto a four-strip, fast x-ray framing camera[28] using a magnification of 6. With this setup, the point-spread function (PSF) of the diagnostic had a diameter at full width at half maximum of $d_{PSF} = 12\ \mu$m. The images were integrated over 40 ps. A 25.4-μm-thick Be filter was used to select the soft x rays above ~1 keV. The absolute timing between the laser pulse and the images was known to an accuracy of 20 ps and the interstrip timing was determined within 5 ps (Refs. 29 and 30).

Figure 147.1(c) shows the x-ray self-emission profile at the beginning of the deceleration of the shell calculated by post-processing the hydrodynamic simulations [Fig. 147.1(b)] with Spect3D.[31] The inner edge of the outer peak generated by the coronal plasma was used to determine the position of the outer surface of the shell, while the outer edge of the central emission (hot spot) was used to determine the position of the inner surface of the shell. The emission of the coronal plasma is maximum near the outer surface of the shell because the plasma has a larger density and the integration distance to the detector is maximum. Just inside the outer surface of the shell, the emission drops by a factor of 2 over a few microns as the emission from the back of the target is absorbed into the cold shell. When the shell begins to decelerate, the pressure of the hot spot rapidly increases ($P_{hs} \propto 1/R^5$), resulting in an increase

in the electron temperature and a rapid start of the emission of x rays from the hot spot with energies above 1 keV. The maximum emission occurs close to the inner edge of the shell, where the shell is ablated and the plasma has a high density. To account for the PSF of the diagnostic, the edge position is measured using the 10% intensity point [$0.1 \times (I_{max} - I_{min}) + I_{min}$, where I_{max} and I_{min} are the maximum and minimum emissions inside the coronal emission]. During the deceleration phase, this outer edge corresponds to the inner side of the cold shell where the temperature drops below 400 eV.

Figure 147.2 shows the self-emission images measured at the end of the laser pulse and at maximum compression. Accurate measurements of the positions of the outer- and inner-shell radii were obtained by averaging the positions of the inner edge of the outer peak and the outer edge of the hot-spot emission determined at each angle. To reduce the noise, self-emission images were angularly averaged over the spatial resolution of the diagnostic ($\theta_{avg} = d_{PSF}/R \approx 20°$, where R is either the outer- or inner-shell radius). With this method, the standard deviation in the variation (as a function of the angle) of the position of the outer edge (inner edge) of the shell was $\sigma_{outer} = \pm2\ \mu$m ($\sigma_{inner} = \pm3\ \mu$m), resulting in an error in the 360° averaged radius of $\delta R_{outer} = \sigma_{outer}/\sqrt{N_p} \approx 0.2\ \mu$m (Ref. 30) ($\delta R_{inner} \approx \pm0.5\ \mu$m), where $N_p = 2\pi R/d_{PSF}$ is the number of independent measurements and R is the averaged radius. To measure the inner-shell radius, an additional error was introduced by the difference between the 10% intensity point and the inner radius. A maximum error of ~2 μm was determined
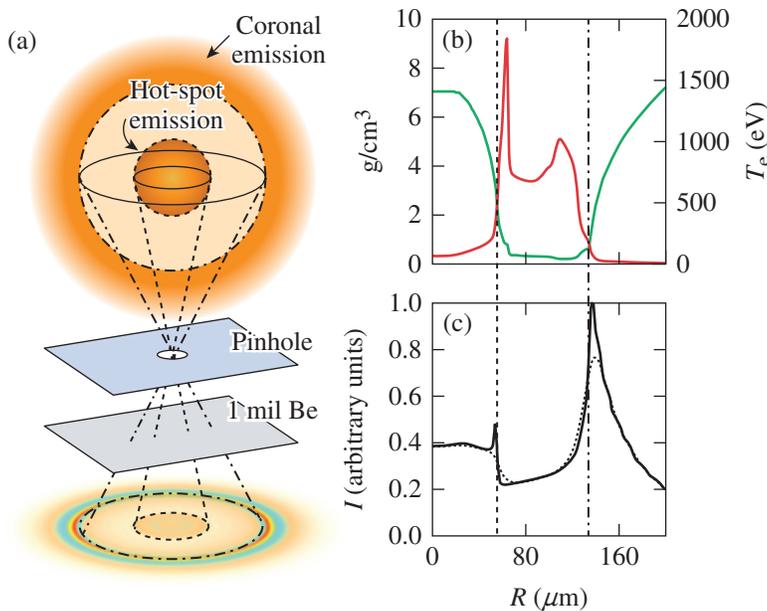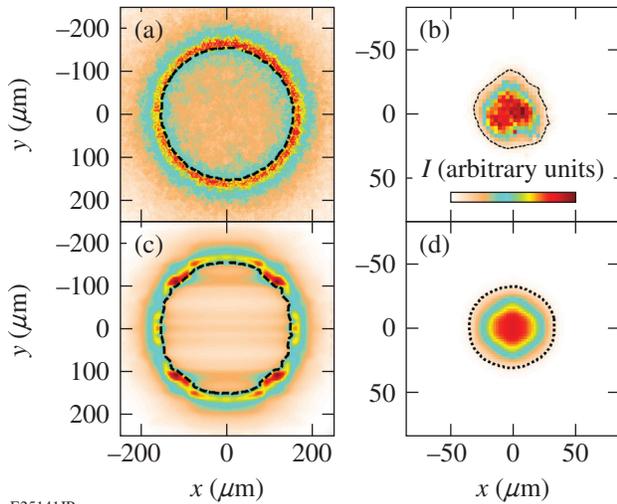

Figure 147.1

(a) The x-ray emission above 1 keV from the coronal plasma and the hot spot was imaged by a pinhole through a Be filter and measured by an x-ray framing camera. A synthetic image calculated for an implosion with an adiabat of 6 is shown. (b) The temperature (green curve) and density profiles (red curve) of the target are compared with the (c) self-emission profiles measured at the diagnostic plane with (dotted curve) and without (solid curve) convolving with the point-spread function (PSF) of the diagnostic. The positions of the outer (dashed–dotted vertical lines) and inner shell (dashed vertical lines) are indicated.
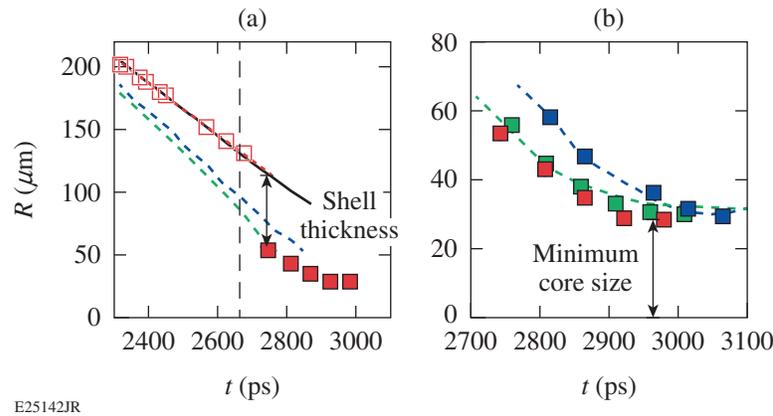
E25140JR

E25141JR

Figure 147.2
Comparisons of the [(a),(b)] measured and [(c),(d)] calculated self-emission images at the end of the laser pulse (2.6 ns) and at the maximum compression (3 ns), respectively. The positions of the [(a),(c)] outer and [(b),(d)] inner shell are shown as dashed black lines and dotted black lines, respectively.

by comparing those two quantities in hydrodynamic simulations performed with and without nonuniformities (Fig. 147.3).

Figure 147.3 shows the simultaneous measurement of the outer and inner surfaces of the shell, which determined the maximum in-flight shell thickness, the deceleration of the shell,

and the minimum core size. Once the laser turned off, the position of the outer surface was determined by extrapolating the measured outer-shell trajectory along a free-fall line. During this time (up to 70 ps), the target was not accelerated by the laser and it imploded with a constant velocity (simulations show that at this time convergence effects are negligible). The 4% error in the measurement of the velocity of the outer shell[30] resulted in a maximum error of ± 1 μm in the inferred outer-shell radius at the beginning of the core emission.

Figure 147.4(a) shows that when SSD was used, the maximum in-flight shell thickness was measured to decrease from 75 μm to 60 μm when the adiabat was decreased from $\alpha = 6$ to $\alpha = 4.5$, but when the adiabat was reduced to $\alpha = 1.8$, the thickness of the shell increased to 75 μm. This is not consistent with the reduction of the shell's adiabat. For each experiment, the measured outer-shell trajectory was nearly identical, indicating that the ablation pressure was similar among these shots. This increase in shell thickness is not explained by an error in the adiabat calculation because the measured minimum core size continued to decrease as the adiabat was reduced [Fig. 147.4(b)] and the neutron yield was up to 5× larger for the lower-adiabat ($\alpha = 1.8$ to $\alpha = 3$) implosions compared with the higher-adiabat ($\alpha = 4.5$ to $\alpha = 6$) implosions [Fig. 147.4(c)]. This is consistent with previous observations that showed a mild reduction in the areal density measured at maximum neutron yield compared to 1-D simulations at low adiabat.[11] The measured increase in

E25142JR

Figure 147.3
(a) The thickness of the shell was determined by the distance between the outer-shell radius (open squares) extrapolated with a constant velocity (short dashed red line) and the inner-shell radius (solid squares) at the time when the hot spot first emits x rays. Once the laser turned off (long black dashed line), the position of the outer surface was determined by extrapolating the measured outer-shell trajectory along a free-fall line. The inner surface trajectory at 1/e of the maximum density was calculated from a simulation without laser imprint (dashed blue curve) and with laser imprint (dashed green curve). For the two simulations, the outer-shell trajectories at 0.2 of the maximum are the same (black curve) and are in excellent agreement with measurements. (b) The measured inner-surface trajectories (red squares) are compared with a 2-D simulations with (green squares) and without (blue squares) laser imprint. The trajectories of the surface where the hot-spot electron temperature drops below 400 eV is plotted for both simulations (dashed curves). The laser beams were smoothed by smoothing by spectral dispersion (SSD) and drove the implosion with $\alpha = 3$, which is slightly larger than the adiabat in the simulation (+2.5) because of the experimental reproducibility.
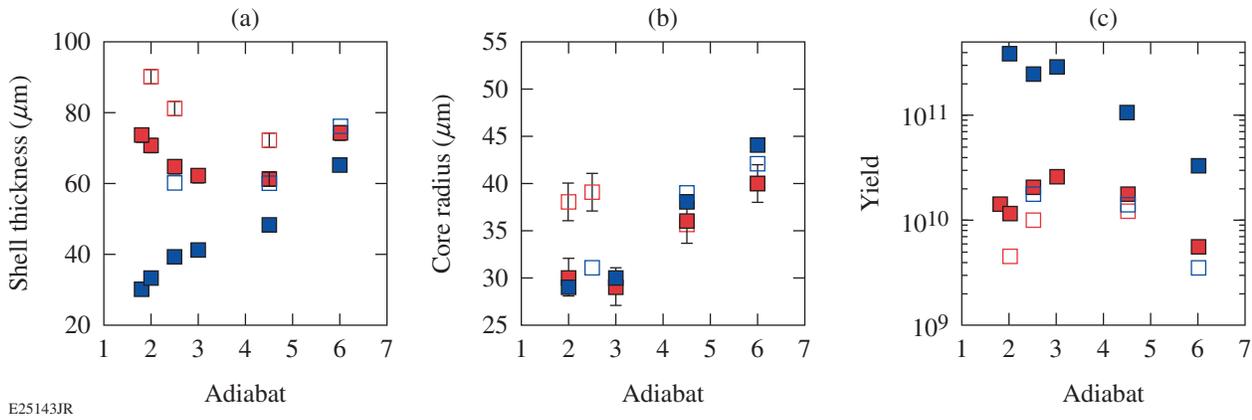
E25143JR

Figure 147.4
(a) The measured shell thicknesses at the beginning of the core emission, (b) core radii at maximum compression, and (c) neutron yields were compared for the different adiabats with (solid red points) and without (open red points) SSD. The corresponding simulations with (open blue squares) and without imprint (solid blue squares) are shown.

the shell thickness for low-adiabat implosions was consistent with an increase in the RT growth that resulted in larger shell nonuniformities, which decompressed the shell.

To understand the shell decompression measured for low-adiabat implosions, hydrodynamic simulations were performed with the 2-D hydrodynamic code *DRACO*[17] using the current state-of-the-art models for nonlocal thermal transport,[32,33] CBET, first-principles equation of state,[34] and laser imprint (including modes between 2 and 200). To resolve both CBET and laser imprint, each simulation required approximately three months of computational time on ~300 cores. Only the shell nonuniformities caused by laser imprint were simulated because the RT growth is dominant for large modes (>100) and the perturbations caused by target roughness are smaller by about a factor of 10 than those imposed by imprint. For all simulations, the trajectory of the outer surface of the shell was well reproduced, indicating that the hydrodynamic efficiency was correctly modeled.[29] Simulations were able to reproduce the maximum in-flight shell thickness, inner-shell deceleration, minimum core size, and neutron yield (Figs. 147.3 and 147.4). This excellent agreement for $\alpha \leq 3$ suggests that the shell decompression measured for low-adiabat implosions was caused by laser imprint. For larger-adiabat implosions, the excellent agreement shows that the reduction in the RT growth with the shell adiabat was correctly modeled. For the lowest-adiabat ($\alpha \leq 2$) implosions, the simulated shell was broken in-flight, which produced a nonphysical hole (i.e., ring) in the shell as a result of the 2-D symmetry. This resulted in a large increase in the final core size and a strong reduction in neutron yield.

The fact that the final core size was significantly smaller for lower-adiabat implosions, even when the maximum in-flight shell thickness was similar, is a result of the laser imprint primarily decompressing the outer surface of the shell. The inner-shell density, and therefore the inner-shell pressure, remained large, leading to a small final core radius.[10] Furthermore, the core pressure was reduced slightly by the RT-induced mix of the CH into the D_2 core, allowing the shell to converge further. For the larger-adiabat implosions, the shell thickness increased because of increased shock heating, resulting in a smaller convergence.

Figure 147.4 shows that hydrodynamic simulations performed without laser imprint (1-D–like) are in better agreement with measurements for high-adiabat shots, but they significantly underestimate the shell thickness for low-adiabat implosions. For $\alpha \leq 3$, these simulations predict that the shell thickness continues to decrease contrary to the experiments. This confirms that the laser imprint causes the decompression of the shell. This increased decompression resulted in an increasing difference between the measured and calculated neutron yields [Fig. 147.4(c)].

When the laser imprint was increased by turning SSD off, the thickness of the shell was increased by ~25%, leading to a reduced neutron yield for each adiabat tested (Fig. 147.4). Compared to SSD-on shots, a weaker degradation of the implosion performances (smaller increase of the core size and smaller reduction in neutron yield) was obtained for a larger adiabat ($\alpha = 4.5$) than for a lower adiabat ($\alpha = 2.5$ and $\alpha = 2$). This is a result of the larger laser imprint that required a stronger mitigation of the RT growth to keep the shell compressible.

In summary, the decompression of an imploding shell was studied by measuring the maximum in-flight shell thicknesses for adiabats ranging from 1.8 to 6 and comparing the results with the first 2-D hydrodynamic simulations, which included laser imprint, nonlocal thermal transport, CBET, and first-principles equation-of-state models. When the adiabat of the shell was decreased, the shell thickness was initially measured to decrease. Reducing the adiabat below 3 resulted in an increasing shell thickness. Over this adiabat scan, the measured minimum core size continued to decrease, showing that the decompression of the shell measured for low adiabats was not caused by errors in the adiabat calculations but by an increase in the RT growth. Hydrodynamic simulations reproduced the measured outer-shell trajectory, maximum in-flight shell thicknesses, inner-shell deceleration, minimum core size, and neutron yields. Simulations that did not include laser imprint were in good agreement with measurements for $\alpha > 3$, but they significantly underestimated the shell thickness for $\alpha \leq 3$, which confirmed that the decompression measured for low adiabats was a result of laser imprint.

ACKNOWLEDGMENT

REFERENCES

1. M. C. Herrmann, M. Tabak, and J. D. Lindl, Phys. Plasmas **8**, 2296 (2001).

2. R. Betti, K. Anderson, V. N. Goncharov, R. L. McCrory, D. D. Meyerhofer, S. Skupsky, and R. P. J. Town, Phys. Plasmas **9**, 2277 (2002)

3. J. Nuckolls *et al*., Nature **239**, 139 (1972).

4. J. D. Lindl, *Inertial Confinement Fusion: The Quest for Ignition and Energy Gain Using Indirect Drive* (Springer-Verlag, New York, 1998).

5. S. E. Bodner, D. G. Colombant, J. H. Gardner, R. H. Lehmberg, S. P. Obenschain, L. Phillips, A. J. Schmitt, J. D. Sethian, R. L. McCrory, W. Seka, C. P. Verdon, J. P. Knauer, B. B. Afeyan, and H. T. Powell, Phys. Plasmas **5**, 1901 (1998).

6. S. E. Bodner, Phys. Rev. Lett. **33**, 761 (1974).

7. V. N. Goncharov, R. Betti, R. L. McCrory, P. Sorotokin, and C. P. Verdon, Phys. Plasmas **3**, 1402 (1996).

8. V. N. Goncharov, J. P. Knauer, P. W. McKenty, P. B. Radha, T. C. Sangster, S. Skupsky, R. Betti, R. L. McCrory, and D. D. Meyerhofer, Phys. Plasmas **10**, 1906 (2003).

9. V. N. Goncharov, T. C. Sangster, T. R. Boehly, S. X. Hu, I. V. Igumenshchev, F. J. Marshall, R. L. McCrory, D. D. Meyerhofer, P. B. Radha, W. Seka, S. Skupsky, C. Stoeckl, D. T. Casey, J. A. Frenje, and R. D. Petrasso, Phys. Rev. Lett. **104**, 165001 (2010).

10. V. N. Goncharov, T. C. Sangster, R. Betti, T. R. Boehly, M. J. Bonino, T. J. B. Collins, R. S. Craxton, J. A. Delettrez, D. H. Edgell, R. Epstein, R. K. Follet, C. J. Forrest, D. H. Froula, V. Yu. Glebov, D. R. Harding, R. J. Henchen, S. X. Hu, I. V. Igumenshchev, R. Janezic, J. H. Kelly, T. J. Kessler, T. Z. Kosc, S. J. Loucks, J. A. Marozas, F. J. Marshall, A. V. Maximov, R. L. McCrory, P. W. McKenty, D. D. Meyerhofer, D. T. Michel, J. F. Myatt, R. Nora, P. B. Radha, S. P. Regan, W. Seka, W. T. Shmayda, R. W. Short, A. Shvydky, S. Skupsky, C. Stoeckl, B. Yaakobi, J. A. Frenje, M. Gatu-Johnson, R. D. Petrasso, and D. T. Casey, Phys. Plasmas **21**, 056315 (2014).

11. P. B. Radha, C. Stoeckl, V. N. Goncharov, J. A. Delettrez, D. H. Edgell, J. A. Frenje, I. V. Igumenshchev, J. P. Knauer, J. A. Marozas, R. L. McCrory, D. D. Meyerhofer, R. D. Petrasso, S. P. Regan, T. C. Sangster, W. Seka, and S. Skupsky, Phys. Plasmas **18**, 012705 (2011).

12. O. A. Hurricane *et al*., Nature **506**, 343 (2014).

13. H. S. Park *et al*., Phys. Rev. Lett. **112**, 055001 (2014).

14. S. P. Regan, R. Epstein, B. A. Hammel, L. J. Suter, J. Ralph, H. Scott, M. A. Barrios, D. K. Bradley, D. A. Callahan, C. Cerjan, G. W. Collins, S. N. Dixit, T. Doeppner, M. J. Edwards, D. R. Farley, S. Glenn, S. H. Glenzer, I. E. Golovkin, S. W. Haan, A. Hamza, D. G. Hicks, N. Izumi, J. D. Kilkenny, J. L. Kline, G. A. Kyrala, O. L. Landen, T. Ma, J. J. MacFarlane, R. C. Mancini, R. L. McCrory, N. B. Meezan, D. D. Meyerhofer, A. Nikroo, K. J. Peterson, T. C. Sangster, P. Springer, and R. P. J. Town, Phys. Plasmas **19**, 056307 (2012).

15. T. Ma, P. K. Patel, N. Izumi, P. T. Springer, M. H. Key, L. J. Atherton, L. R. Benedetti, D. K. Bradley, D. A. Callahan, P. M. Celliers, C. J. Cerjan, D. S. Clark, E. L. Dewald, S. N. Dixit, T. Döppner, D. H. Edgell, R. Epstein, S. Glenn, G. Grim, S. W. Haan, B. A. Hammel, D. Hicks, W. W. Hsing, O. S. Jones, S. F. Khan, J. D. Kilkenny, J. L. Kline, G. A. Kyrala, O. L. Landen, S. Le Pape, B. J. MacGowan, A. J. Mackinnon, A. G. MacPhee, N. B. Meezan, J. D. Moody, A. Pak, T. Parham, H.-S. Park, J. E. Ralph, S. P. Regan, B. A. Remington, H. F. Robey, J. S. Ross, B. K. Spears, V. Smalyuk, L. J. Suter, R. Tommasini, R. P. Town, S. V. Weber, J. D. Lindl, M. J. Edwards, S. H. Glenzer, and E. I. Moses, Phys. Rev. Lett. **111**, 085004 (2013).

16. T. C. Sangster, V. N. Goncharov, R. Betti, P. B. Radha, T. R. Boehly, D. T. Casey, T. J. B. Collins, R. S. Craxton, J. A. Delettrez, D. H. Edgell, R. Epstein, C. J. Forrest, J. A. Frenje, D. H. Froula, M. Gatu-Johnson, V. Yu. Glebov, D. R. Harding, M. Hohenberger, S. X. Hu, I. V. Igumenshchev, R. Janezic, J. H. Kelly, T. J. Kessler, C. Kingsley, T. Z. Kosc, J. P. Knauer, S. J. Loucks, J. A. Marozas, F. J. Marshall, A. V. Maximov, R. L. McCrory, P. W. McKenty, D. D. Meyerhofer, D. T. Michel, J. F. Myatt, R. D. Petrasso, S. P. Regan, W. Seka, W. T. Shmayda, R. W. Short, A. Shvydky, S. Skupsky, J. M. Soures, C. Stoeckl, W. Theobald, V. Versteeg, B. Yaakobi, and J. D. Zuegel, Phys. Plasmas **20**, 056317 (2013).

17. P. B. Radha, T. J. B. Collins, J. A. Delettrez, Y. Elbaz, R. Epstein, V. Yu. Glebov, V. N. Goncharov, R. L. Keck, J. P. Knauer, J. A. Marozas, F. J. Marshall, R. L. McCrory, P. W. McKenty, D. D. Meyerhofer, S. P. Regan, T. C. Sangster, W. Seka, D. Shvarts, S. Skupsky, Y. Srebro, and C. Stoeckl, Phys. Plasmas **12**, 056307 (2005).

18. S. X. Hu, P. B. Radha, J. A. Marozas, R. Betti, T. J. B. Collins, R. S. Craxton, J. A. Delettrez, D. H. Edgell, R. Epstein, V. N. Goncharov, I. V. Igumenshchev, F. J. Marshall, R. L. McCrory, D. D. Meyerhofer, S. P. Regan, T. C. Sangster, S. Skupsky, V. A. Smalyuk, Y. Elbaz, and D. Shvarts, Phys. Plasmas **16**, 112706 (2009).

19. S. X. Hu, V. N. Goncharov, P. B. Radha, J. A. Marozas, S. Skupsky, T. R. Boehly, T. C. Sangster, D. D. Meyerhofer, and R. L. McCrory, Phys. Plasmas **17**, 102706 (2010).

20. D. T. Michel, A. K. Davis, V. N. Goncharov, T. C. Sangster, S. X. Hu, I. V. Igumenshchev, D. D. Meyerhofer, W. Seka, and D. H. Froula, Phys. Rev. Lett. **114**, 155002 (2015).

21. S. X. Hu, D. T. Michel, A. K. Davis, R. Betti, P. B. Radha, E. M. Campbell, D. H. Froula, and C. Stoeckl, "Understanding the Effects of Laser Imprint on Plastic-Target Implosions on OMEGA," to be published in Physics of Plasmas.

22. J. A. Marozas and T. J. B. Collins, Bull. Am. Phys. Soc. **57**, 344 (2012).

23. T. R. Boehly, D. L. Brown, R. S. Craxton, R. L. Keck, J. P. Knauer, J. H. Kelly, T. J. Kessler, S. A. Kumpan, S. J. Loucks, S. A. Letzring, F. J. Marshall, R. L. McCrory, S. F. B. Morse, W. Seka, J. M. Soures, and C. P. Verdon, Opt. Commun. **133**, 495 (1997).

24. T. R. Boehly, V. A. Smalyuk, D. D. Meyerhofer, J. P. Knauer, D. K. Bradley, R. S. Craxton, M. J. Guardalben, S. Skupsky, and T. J. Kessler, J. Appl. Phys. **85**, 3444 (1999).

25. S. Skupsky, R. W. Short, T. Kessler, R. S. Craxton, S. Letzring, and J. M. Soures, J. Appl. Phys. **66**, 3456 (1989).

26. T. J. Kessler, Y. Lin, J. J. Armstrong, and B. Velazquez, Proc. SPIE **1870**, 95 (1993).

27. D. T. Michel, C. Sorce, R. Epstein, N. Whiting, I. V. Igumenshchev, R. Jungquist, and D. H. Froula, Rev. Sci. Instrum. **83**, 10E530 (2012).

28. D. K. Bradley, P. M. Bell, J. D. Kilkenny, R. Hanks, O. Landen, P. A. Jaanimagi, P. W. McKenty, and C. P. Verdon, Rev. Sci. Instrum. **63**, 4813 (1992).

29. D. T. Michel, V. N. Goncharov, I. V. Igumenshchev, R. Epstein, and D. H. Froula, Phys. Rev. Lett. **111**, 245005 (2013).

30. D. T. Michel, A. K. Davis, W. Armstrong, R. Bahr, R. Epstein, V. N. Goncharov, M. Hohenberger, I. V. Igumenshchev, R. Jungquist, D. D. Meyerhofer, P. B. Radha, T. C. Sangster, C. Sorce, and D. H. Froula, High Power Laser Science and Engineering **3**, e19 (2015).

31. J. J. MacFarlane *et al.*, High Energy Density Phys. **3**, 181 (2007).

32. G. P. Schurtz, Ph. D. Nicolaï, and M. Busquet, Phys. Plasmas **7**, 4238 (2000).

33. D. Cao, G. Moses, and J. Delettrez, Phys. Plasmas **22**, 082308 (2015).

34. S. X. Hu, L. A. Collins, V. N. Goncharov, J. D. Kress, R. L. McCrory, and S. Skupsky, Phys. Rev. E **92**, 043104 (2015).